








RESEARCH ARTICLE | MAY 14 2024

Development and calibration of a multi-delay coherence imaging diagnostic on the MAST-U tokamak

R. S. Doyle ; N. Lonigro ; J. S. Allcock ; S. A. Silburn ; M. M. Turner ; X. Feng ; H. Leggate 



Rev. Sci. Instrum. 95, 053505 (2024)

<https://doi.org/10.1063/5.0205584>



Articles You May Be Interested In

Calibration of coherence imaging spectroscopy using spectral line sources

Rev. Sci. Instrum. (July 2021)

Laser calibration of the DIII-D coherence imaging system

Rev. Sci. Instrum. (September 2018)

Multi-delay coherence imaging spectroscopy optimized for ion temperature measurements in the divertor plasma of the Wendelstein 7-X stellarator

Rev. Sci. Instrum. (July 2024)



Special Topics Open for Submissions

[Learn More](#)

Development and calibration of a multi-delay coherence imaging diagnostic on the MAST-U tokamak

Cite as: Rev. Sci. Instrum. 95, 053505 (2024); doi: 10.1063/5.0205584

Submitted: 27 February 2024 • Accepted: 25 April 2024 •

Published Online: 14 May 2024



R. S. Doyle,^{1,a)} N. Lonigro,^{2,3} J. S. Allcock,² S. A. Silburn,² M. M. Turner,¹ X. Feng,^{4,5}
and H. Leggate¹

AFFILIATIONS

¹ National Centre for Plasma Science and Technology, Dublin City University, Dublin, Ireland

² United Kingdom Atomic Energy Authority, Culham Centre for Fusion Energy, Culham Science Centre, Abingdon, Oxon OX14 3DB, United Kingdom

³ York Plasma Institute, University of York, York YO10 5DQ, United Kingdom

⁴ Centre for Advanced Instrumentation, Department of Physics, Durham University, South Road, Durham DH1 3LE, United Kingdom

⁵ General Fusion, Inc., 6020 Russ Baker Wy, Richmond, British Columbia V7B 1B4, Canada

^{a)} Author to whom correspondence should be addressed: rhys.sd@protonmail.com

ABSTRACT

The MAST-U Super-X divertor provides the opportunity to study fusion plasma exhaust under novel conditions. However, in order to study these conditions, advanced diagnostics are required. Following the development of the MAST-U Multi-Wavelength Imaging (MWI) diagnostic, we present the installation of a multi-delay coherence imaging spectroscopy (CIS) system within the MAST-U MWI, along with modifications made to the MWI for effective operation. This diagnostic will measure either carbon ion flow velocities and temperatures or electron densities through D_γ emission. We have extended previously developed techniques for wavelength calibration to account for errors due to the misalignment of interferometer components. In addition, we have developed a comprehensive calibration procedure to account for the temperature dependence of the instrument's delays by fitting to a linearly modified version of the delay equation presented by Veiras *et al.* [Appl. Opt. 49(15), 2769 (2010)]. Together, these procedures reduce the cost and hardware complexity of implementing CIS instruments when compared to those that use *in situ* or tunable laser calibration systems, as calibrations can be generated to good accuracy using previously measured data.

© 2024 Author(s). All article content, except where otherwise noted, is licensed under a Creative Commons Attribution-NonCommercial 4.0 International (CC BY-NC) license (<https://creativecommons.org/licenses/by-nc/4.0/>). <https://doi.org/10.1063/5.0205584>

I. INTRODUCTION

The Super-X divertor configuration¹ for tokamak fusion devices has been proposed as a solution to the significant challenge of heat and particle exhaust^{2,3} in magnetic confinement fusion. In order to study the effects of this configuration, a Super-X divertor was installed on the spherical tokamak MAST-Upgrade (MAST-U).⁴ This created a need for improved diagnostic coverage of the MAST-U divertor. The Multi-Wavelength Imaging (MWI) diagnostic was developed and installed on MAST-U⁵ for this purpose. This multi-channel optical cavity polychromator system is capable

of imaging 11 distinct spectral lines, simultaneously, which allows for in-depth physical studies. The MWI was also designed to host a coherence imaging spectroscopy (CIS) system.

Coherence imaging spectroscopy is a narrowband spectral imaging diagnostic, which measures the emission of a plasma and provides an image of its lower-order spectral moments, which can be used to infer, for example, spectral line shift or broadening over a 2D field of view.

Unlike traditional interferometers, such as the one created by Michelson, coherence imaging systems split the amplitude of incoming light into two orthogonal polarization states with different

optical path lengths. The coherence of these orthogonal rays can then be measured via the interference pattern produced, which is superimposed on a line-integrated intensity image of the plasma. The pattern is related to the spectrum of the incoming light through the principles of Fourier transform spectroscopy. The general form of intensity of this pattern is given by Eq. (1), where $g(\nu)$ is the emission spectrum of the plasma at frequency ν and ϕ is the optical path length difference, which varies across the imaging sensor. This is known as a spatially multiplexed design and is the most common type of CIS system, first used on the H-1 heliac,⁶

$$I(\phi, \nu) = g(\nu)[1 + \cos(\nu\phi)]. \quad (1)$$

The interference pattern is created by birefringent crystal(s) placed between polarizers in the collimated region of the imaging system. The spectral and spatial responses of the interferometer can be changed by modifying the number of interferometer components or their relative orientations. A single-delay system produces an interference pattern at a single spatial carrier frequency, commonly as a linear delay shear⁷ or using pixelated sensor,⁸ whereas multi-delay systems sample at multiple fixed delays. The use of multiple delays is advantageous when measuring complicated spectra, such as the multiplet of C III, or in the case where multiple broadening mechanisms may exist. In these cases, the spectral response of the instrument is more complicated, thus requiring multiple delays to make interpretation of results easier and reduce systematic errors, when compared to single delay systems. Multi-delay measurements have been performed by using a single-delay system and repeating plasmas with different crystal thicknesses,⁹ or in one interferometer using multiple crystals, which encode each delay at a different spatial frequency.¹⁰

As with all diagnostics, accurate calibrations are imperative for effective physical studies. With CIS systems, we must mitigate against the temperature dependence of the delay imparted by the crystals. To do this, frequent measurements of the following quantities are required:

- Group delay ($\hat{\phi}$): the effective interferometer path delay accounting for dispersion in the crystals to first order.
- Rest frame phase (ϕ_0): the phase that corresponds to a flow velocity of 0 km/s.
- Instrumental contrast (ζ_I): the contrast measured by the instrument in the presence of an ideal infinitely narrow spectral line.

This has been achieved on W7-X¹¹ and DIII-D¹² with an *in situ* tunable laser. However, *in situ* systems are not always practical and tunable lasers are expensive, negating the cost-effectiveness of CIS systems. Herein, we present calibration techniques that aim to reduce the CIS operational complexity while maintaining its cost-effective nature. We do this by extending previously developed wavelength fitting procedures,¹³ in which the dispersion of a crystal is characterized by fitting instrument parameters to phase measurements taken at multiple wavelengths. This method negates the need for a tunable laser at the specific wavelength of interest. In addition, we present a temperature characterization method, which negates the need for an *in situ* calibration system to account for calibration drifts with ambient and crystal temperature changes.

In Sec. II, an outline of the CIS system installed in the MWI for the second MAST-U campaign will be given. Also described are the challenges and solutions to image ghosting and the existence of two CIS focal planes, which are associated with using a polarization interferometer within a polychromator. In Sec. III, we present an extension to the wavelength calibration method presented by Allcock *et al.*¹³ to ensure accurate calibration of CIS systems when a coherent light source at the exact wavelength of interest is not available. Section IV presents a method to characterize the temperature dependence of a given CIS system, thus reducing the frequency at which calibrations need to be executed. Finally, Sec. V summarizes these calibration methods.

II. MULTI-DELAY COHERENCE IMAGING ON MAST-U

The interference pattern created by a coherence imaging spectroscopy system is defined by two quantities, its phase and its contrast, measured at each pixel. In multi-delay systems, each delay has its own interference pattern and, therefore, its own phase and contrast images. To perform physical studies, a relation between these quantities and the normalized plasma emission spectrum, $g(\nu)$, is required. Equation (2) shows how the degree of temporal coherence,¹⁴ $\gamma(\phi_{0,n})$, of the light incident on the sensor relates to $g(\nu)$, where ν_0 is the center-of-mass frequency of the spectrum and κ_0 is the dispersion coefficient of the instrument. This can then be related to measured contrast, ζ_n , and measured phase, Φ_n , through Eq. (3), where $\phi(\hat{\phi}_n)$ and $\zeta(\hat{\phi}_n)$ are the contributions from physical processes to the measured phase and contrast, respectively, and n denotes the delay index (relevant only for multi-delay systems). The rest frame phase and instrumental contrast, which are 2D quantities that must be measured experimentally when calibrating the instrument, will henceforth be denoted by $\phi_{0,n}$ and $\zeta_{I,n}$, respectively,

$$\gamma(\phi_{0,n}) \approx \int_{-\infty}^{\infty} g(\nu) \exp\left(i\phi_{0,n}\left[1 + \kappa_0\left(\frac{\nu - \nu_0}{\nu}\right)\right]\right) d\nu, \quad (2)$$

$$\begin{aligned} \Phi_n &\equiv \arg(\gamma(\phi_{0,n})) = \phi_{0,n} + \phi(\hat{\phi}_n), \\ \zeta_n &= \zeta_{I,n} |\gamma(\phi_{0,n})| = \zeta_{I,n} \zeta(\hat{\phi}_n). \end{aligned} \quad (3)$$

As this technique encodes the spectrum of the plasma in the interference pattern, changes to that spectrum by physical processes result in a deviation from a known reference pattern. Through this, CIS has been used on fusion experiments to measure impurity ion flows via Doppler shift,^{15–17} impurity ion temperatures via Doppler broadening,¹⁸ and electron densities via Stark broadening.⁸ Broadening mechanisms result in a decrease in the measured contrast, whereas a Doppler shift of the spectrum changes the measured phase.

In this study, we present the installation of a triple-delay coherence imaging system on MAST-U, which is based on the quad-delay system developed by Allcock *et al.*⁸ We employ two different types of birefringent crystal, a displacer plate and a high-order waveplate. In decreasing the number of delays measured to 3, we benefit from a factor of $\sqrt{2}$ increase in light throughput compared to a quad-delay system. The displacer plate, which is functionally identical to the Savart plate-waveplate combination used in other

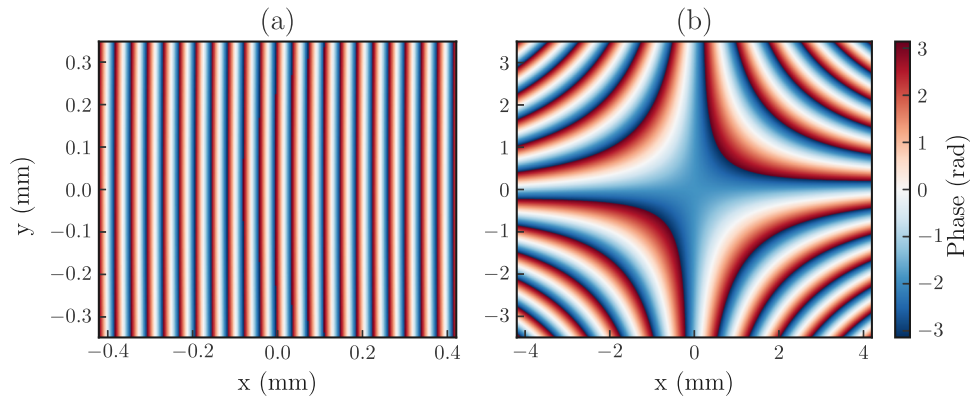


FIG. 1. Phase shift, ϕ imparted by (a) an 8 mm displacer plate with a cut-angle of 45° and (b) a 9.8 mm waveplate. (a) has been zoomed into the center of the sensor by a factor of 10 to resolve the phase shear pattern.

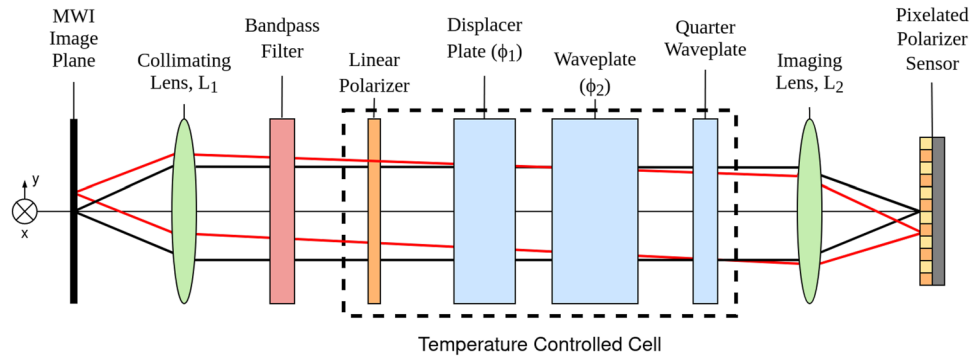


FIG. 2. Schematic of the triple-delay pixelated MWI CIS interferometer setup.

CIS instruments,^{16,19} has a cut-angle, θ (the angle between its optic axis and the crystal face), which is between 0° and 90° , producing a delay shear across the sensor. The waveplate has a cut-angle of 0° , which produces a hyperbolic phase pattern. Both patterns can be

seen in Fig. 1. A linear polarizer is needed at the front of the system to allow the system to act as an interferometer. The interference pattern is then resolved using the zero-order quarter waveplate (QWP) and a polarized camera sensor, as shown in Fig. 2,

$$\phi = \frac{2\pi L}{\lambda} \left(\sqrt{n_O^2 - n_E^2 \sin^2 \alpha} + \frac{n(n_O^2 - n_E^2) \sin \theta \cos \theta \cos \delta \sin \alpha}{n_E^2 \sin^2 \theta + n_O^2 \cos^2 \theta} - \frac{n_O \sqrt{n_E^2 (n_E^2 \sin^2 \theta + n_O^2 \cos^2 \theta) - n^2 \sin^2 \alpha (n_E^2 - (n_E^2 - n_O^2) \cos^2 \theta \sin^2 \delta)}}{n_E^2 \sin^2 \theta + n_O^2 \cos^2 \theta} \right). \quad (4)$$

In order to create three distinct delays, the interferometer components are oriented with respect to the horizontal as shown in Fig. 3(a). Linearly polarized light enters the first crystal, an 8 mm alpha barium borate (α -BBO) crystal with a cut-angle θ of 45° . This

crystal splits the light into two components, an ordinary ray and an extraordinary ray with a delay, ϕ_1 , imposed on the latter. Similarly, the second crystal is a 9.8 mm α -BBO crystal with a cut-angle of 0° producing a delay, ϕ_2 . The magnitude of these delays can be

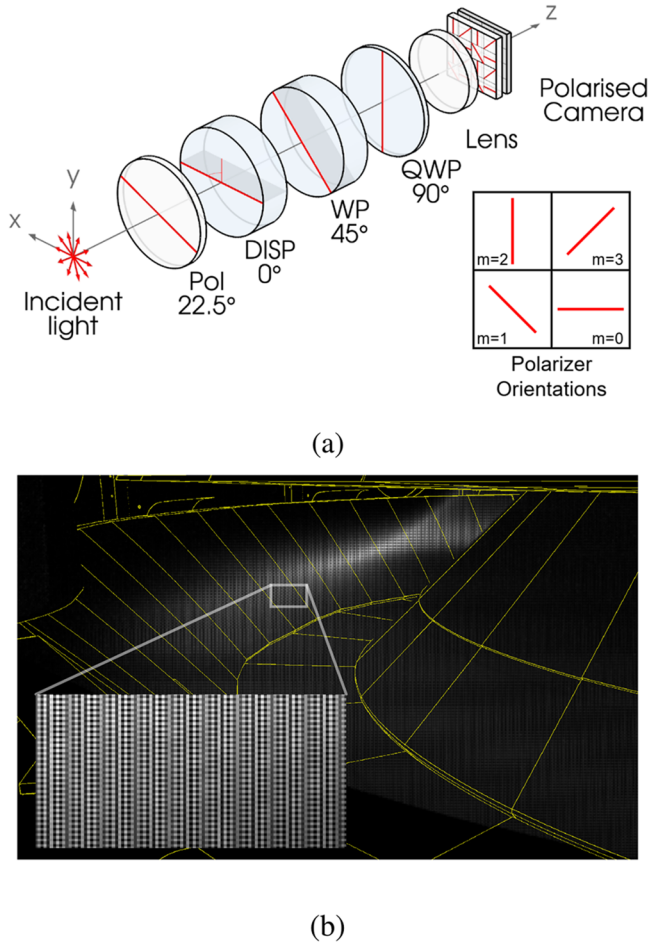


FIG. 3. (a) Orientation of the CIS components within the temperature controlled cell in order to create three distinct delays. Also shown is the orientation of each sensor polarizer within the 2×2 grid. (b) Simulated triple-delay CIS image of a MAST-U plasma in its Super-X divertor configuration showing the combination of both the pixelated and phase shear patterns and the CAD wireframe of the MAST-U divertor.

calculated using Eq. (4).²⁰ The measured image, Fig. 3(b), will then be the sum of three interferograms corresponding to the delays ϕ_2 , $\phi_{2+1} = \phi_2 + \phi_1$, and $\phi_{2-1} = \phi_2 - \phi_1$.

The distinctive checkerboard pattern seen in the interferogram, Fig. 3(b), is due to the polarized sensor of the camera, a FLIR Blackfly S. The sensor polarizers are arranged in a 2×2 grid, as shown in Fig. 3(a), which is repeated across the sensor. The orientation of the transmission axis of each pixel's polarizer is given by $\rho_{pm} = m\frac{\pi}{4}$, where $m \in \{0, 1, 2, 3\}$ is the pixel index within the 2×2 array. In order to limit the effect of ambient temperature changes on the system, the main interferometer components [Fig. 3(a)] are installed within a temperature-controlled cell set at $35^\circ \pm 0.2^\circ\text{C}$. The effects of crystal temperature on interferometer delays are discussed further in Sec. IV.

The equation for the interferogram produced by this instrument can be found using Mueller calculus, where the Mueller matrix

of the instrument is given by Eq. (5). The definition of each matrix can be found in Appendix A. It can subsequently be shown that using the Stokes vector for unpolarized light as the input, the irradiance measured at the camera sensor is given by Eq. (6). The measured interferogram, I_{out} , can then be demodulated, via the process of *synchronous demodulation* described by Allcock,^{8,10} to extract the phase (Φ_n) and contrast (ζ_n) images,

$$\mathbf{M}_{tot} \equiv \mathbf{M}_{pol}\left(m\frac{\pi}{4}\right) \times \mathbf{M}_{qwp}\left(\frac{\pi}{2}\right) \times \mathbf{M}_{ret}\left(\frac{\pi}{4}, \phi_2\right) \times \mathbf{M}_{ret}(0, \phi_1) \times \mathbf{M}_{pol}\left(\frac{\pi}{8}\right), \quad (5)$$

$$I_{out} = \frac{I_{in}}{4} \left(1 + \frac{\sqrt{2}}{2} \zeta_2 \cos\left(\Phi_2 + m\frac{\pi}{2}\right) + \frac{\sqrt{2}}{4} \zeta_{2-1} \cos\left(\Phi_{2-1} + m\frac{\pi}{2}\right) - \frac{\sqrt{2}}{4} \zeta_{2+1} \cos\left(\Phi_{2+1} + m\frac{\pi}{2}\right) \right). \quad (6)$$

The MAST-U CIS system has been installed within the MAST-U MWI diagnostic.^{5,21} The MWI, shown in Fig. 4, is an 11-channel optical cavity polychromator capable of imaging 11 distinct spectral lines using different spectral bandpass filters.

A. CIS focus planes

Light incident on each MWI camera first passes through nine lenses, of which all have manufacturer-quoted focal length tolerances of $\sim 1\%$. This results in a range of possible locations at which the intermediate image of each channel is formed, causing imperfect collimation of incoming light. This is not an issue for the MWI as each channel's imaging lens is focused individually using a target reticule; however, this is not acceptable for coherence imaging systems.

In collimating the light source, we map each pixel on the camera to a different angle of incidence with respect to the optical axis, z , and the horizontal, x ; therefore, all light from a given spatial location

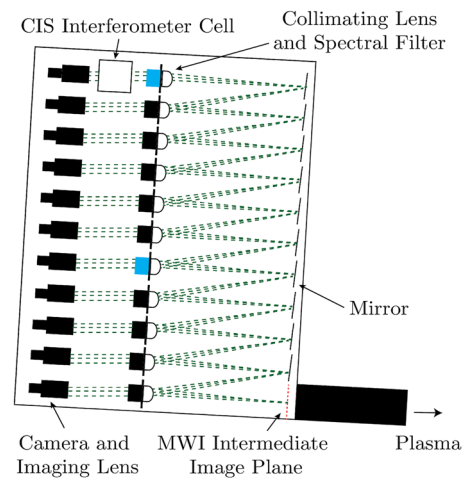


FIG. 4. Schematic of the MAST-U MWI, where the spectral filters marked in blue indicate that the CIS measures the same spectral line as that MWI channel.

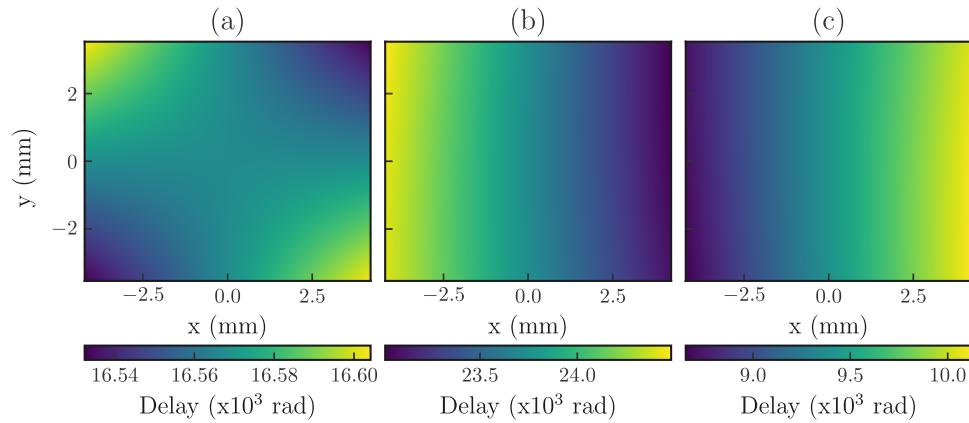


FIG. 5. Modeled delays imparted by each component of the CIS interferometer at 464.7 nm assuming thin lenses. (a) Waveplate only, ϕ_2 , (b) sum of crystal delays, ϕ_{2+1} , and (c) difference between crystal delays, ϕ_{2-1} .

in the image experiences an identical delay but a different delay to all other spatial locations, Fig. 5. If effective collimation is not achieved and the imaging lens of the system is focused to the plasma, light from the same plasma location will experience different interferometer delays. This will appear as an additional broadening of the spectral shape through a reduction in instrumental contrast. Conversely, the instrumental contrast can be maximized by focusing the imaging lens to the interference fringes. In this instance, the plasma would now be out of focus, resulting in a decrease in spatial resolution. In both cases, a reduction in instrument performance is observed.

To achieve acceptable image focus and instrumental contrast, the standard 750 mm focal length collimating lens of the MWI was replaced with a 600 mm lens on the CIS channel to correct for the discrepancy in the intermediate image location. In this configuration, instrumental contrasts of 0.95, 0.7, and 0.6 were measured

for ζ_2 , ζ_{2+1} , and ζ_{2-1} , respectively, while maintaining good image focus.

B. CIS ghosting

The spectral emission lines of interest for electron density and impurity studies on MAST-U using CIS are D_γ (434 nm) and C III (465 nm), respectively, of which both are also measured in the MWI. As the MAST-U MWI cameras are capable of operating at 400–800 Hz compared to the ~ 150 Hz of the CIS, it is advantageous to run both systems simultaneously. Therefore, a 50/50 beam splitter was required on the MWI channel measuring the same spectral line. This was placed after the MWI spectral bandpass filter but before the imaging lens, so other spectral channels are not affected by multiple planes of reflection. However, this led to ghosting on the CIS channel, Fig. 6(a). By intentionally misaligning the beam splitter to different degrees so that the beam splitter and filter faces were not parallel, it was determined that a small misalignment was the cause of this ghosting. As the spectral filter does not have a transmission ratio of 100% or an anti-reflective coating on its rear face, double reflections likely occur between the two components. Because these components are in the collimated region, the effect of double reflections should be negligible. However, if the component surfaces are not parallel to one another, the propagation angle of the light with respect to the collimating lens will change, thus mapping the light to a different spatial location when it passes back through the lens, Fig. 7.

This effect was mitigated by installing the beam splitter so that it was in contact with the spectral filter, thus reducing the air gap to near zero and ensuring that both components were aligned, Fig. 6(b). This was confirmed by comparing Fig. 6(b) to the same image taken when the MWI channel filter–beam splitter pair was replaced with a mirror, which can be thought of as the *ideal* case. To avoid ghosting in future imaging diagnostics of this type, we suggest that the first spectral filter be produced with a transmission ratio of 50%, removing the need for a beam splitter, while the filter on the CIS channel can have a ratio of 100%.

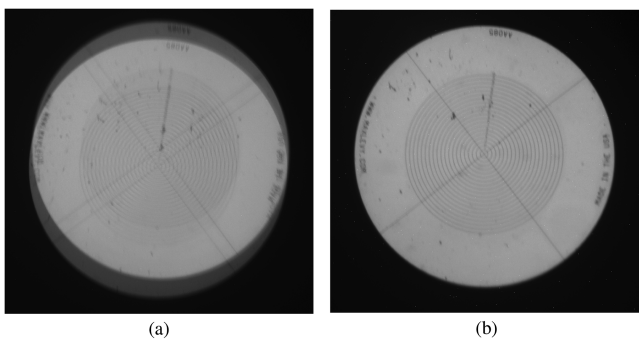


FIG. 6. (a) Ghosting observed on the CIS channel due to misalignment. (b) Ghosting is no longer visible after decreasing the distance between the beam splitter and spectral filter.

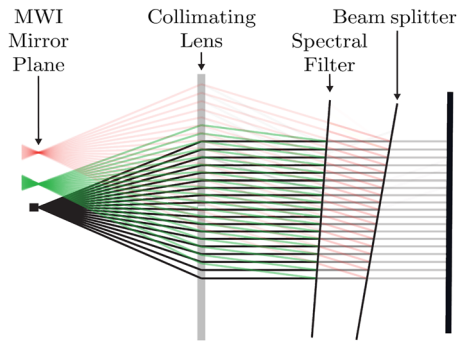


FIG. 7. Using a point source (black), we show that when the beam splitter and spectral filter are not aligned, the light reflecting off the beam splitter (red) is imaged to a different location to that reflected off the spectral filter (green).

III. SPECTRAL CALIBRATION

To obtain accurate calibrations of rest frame phase, $\phi_{0,n}$, a coherent light source at the exact wavelength of interest is required. For lines that do not emit brightly under the conditions of small gas-discharge lamps, a tunable laser is required. To solve this problem, a method of fitting instrument parameters, including Sellmeier coefficients, of the CIS instrument to a set of phase images taken at various wavelengths was developed by Allcock *et al.*¹³ This allows us to characterize the wavelength dependence of each crystal's delay, thus allowing accurate calculations of group delay, $\hat{\phi}_0$, and phase difference, $\Delta\phi$, expected between the wavelength of interest and a close-by (± 5 nm) measured wavelength.

While undertaking this calibration, an unexpected structure in the fit residuals for each delay component was found, Fig. 8, which is not accounted for by our model at the time. We suspected that this hyperbolic pattern may be due to a small rotational misalignment of the interferometer components about the optical axis with respect to each other. Henceforth, any description of a

component's *misalignment* will refer to a rotational misalignment of that component about the CIS instrument's optical axis. This was confirmed as a feasible explanation for the effect by comparing Fig. 8(a) to the corresponding ϕ_2 fit residual image modeled with a 5.8° misalignment of the waveplate, Fig. 8(b), using Mueller calculus. In practice, each component in the system will contribute to this effect; therefore, the real misalignment is likely to be smaller than in Fig. 8(b).

The source of any such misalignment is believed to be a combination of human error and limitations in component mounting. Each component is mounted in a metal cog, which fits inside the temperature controlled cell. The fast-axis (retarders) or polarization axis (polarizer) is aligned with the center of one of the cog notches. This process is done manually and is, therefore, subject to human error, which we estimate could be up to 5° . In addition, it is not possible to fix any possible misalignment, while the components are in the cell as each component can only be rotated by $22.5^\circ \pm 1^\circ$. By misaligning any given component, light which would normally destructively interfere now only partially interferes, which creates this pattern. To see if this kind of misalignment can produce a good quantitative match to our measurements and thus produce accurate interferometer calibrations, we endeavored to include it in the model we are using to fit to the data.

Under the ideal conditions described in Sec. II, the measured phase images are given by $\Phi_2 = \phi_2$ and $\Phi_{2\pm 1} = \phi_2 \pm \phi_1$, wrapped in the interval $(-\pi, \pi]$ rad. However, the analysis of Eq. (5) has found that the misalignment of any component in the instrument introduces additional spatial frequency components at each measured delay whose amplitudes change with the degree of misalignment. Accounting for this could be achieved by calculating the Mueller product at every iteration; however, a factor of 5 increase in computational time was measured. As this process would produce an interferogram not the phase directly, implementation would also require an automatic demodulation algorithm to be developed and executed at each iteration, as the carrier locations in frequency space vary with the orientation each component. Due to this computational complexity and expense of computing, analytical equations

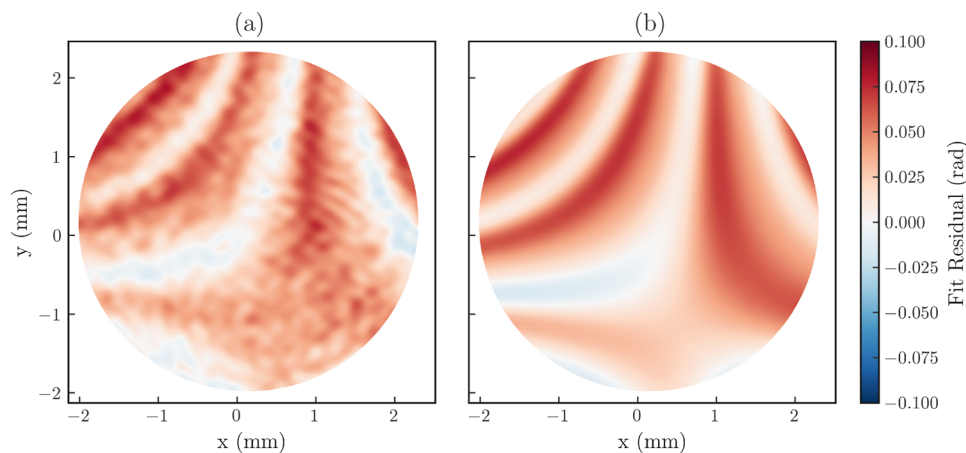


FIG. 8. (a) Residual produced on ϕ_2 when fitting instrument parameters to data taken at 467.82 nm, showing a clear hyperbolic pattern that is not being accounted for. (b) Residual produced when fitting to a synthetic ϕ_2 image at 467.82 nm calculated using an instrument whose waveplate has been misaligned by 5.8° .

that would skip the calculation of an interferogram, instead directly producing phase images, were sought.

As ϕ_2 is directly measured, the orientation of the waveplate can be determined. We can, therefore, measure the misalignment of each other component relative to waveplate orientation (i.e., $\delta_{wp} = 0$). In addition, any misalignment is believed to be small; therefore, the small angle approximation has been used. With this and using Mueller calculus, we have derived equations for the measured phase delays Φ_2 , Φ_{2+1} , and Φ_{2-1} , Eqs. (7)–(9), where δ is the misalignment of a given component, θ_{rot} is the angle in radians at which the entire instrument is rotated with respect to the horizontal axis of the camera sensor, and η_{\mp} is a complex constant related to the misalignment of the polarizer, displacer plate, and quarter waveplate. The sign of the two terms in Eq. (10) is reversed for Φ_{2+1} and Φ_{2-1} compared to Φ_2 ; for example, for η_{-} , the signs are $-$ and $+$. In Eqs. (7)–(9), we have dropped the $\frac{\sqrt{2}}{2}$ and $\frac{\sqrt{2}}{4}$ coefficients seen in Eq. (6) as these have no effect on phase. In the ideal aligned case (i.e., where $\delta_{pol} = \delta_{disp} = \delta_{qwp} = \theta_{rot} = 0$), we can see that the measured phase exactly equals the delay (or combination of delays) imparted by the crystals. A further explanation of the derivation of these equations can be found in Appendix B,

$$\Phi_2 = \arg\left(\left[e^{i\phi_2} + 4\delta_{disp}\delta_{qwp}\right]\eta_{-}\right) - 2\theta_{rot}, \quad (7)$$

$$\Phi_{2+1} = \arg\left(\left[e^{i\phi_{2+1}}(2\delta_{disp} + 1) - 2\delta_{qwp}e^{i\phi_1}\right]\eta_{+}\right) - 2\theta_{rot}, \quad (8)$$

$$\Phi_{2-1} = \arg\left(\left[e^{i\phi_{2-1}}(2\delta_{disp} - 1) - 2\delta_{qwp}e^{-i\phi_1}\right]\eta_{+}\right) - 2\theta_{rot}, \quad (9)$$

$$\eta_{\mp} = (1 \mp 2\delta_{pol} + \delta_{disp}(\pm 2 + 4\delta_{pol}))(1 - 2i\delta_{qwp}). \quad (10)$$

To test our ability to predict phase at given wavelength, phase measurements were taken at five wavelengths using different spectral filters, 434, 467.82, 472.2, 480, and 508 nm. These wavelengths were chosen due to the availability of cadmium, zinc, and hydrogen lamps and due to the proximity of their spectral lines to the wavelength of interest for MAST-U, C III, at 464.7 nm. To ensure that a solution could be found accurately and within a reasonable time period, the fit was performed against the difference between the phase images at the above wavelengths and that measured at 467.82 nm, for example image 1 would be the difference in the phase images taken at 434 and 467.82 nm. The data taken at 472.2 nm were reserved for testing as the wavelength difference between it and Cd 467 is similar to that of C III, while the other wavelength was used for fitting. Tables I and II show the nominal and optimized instrument parameters fit to using Eqs. (7)–(9).

The accuracy of this fitting was then verified by calculating the phase difference for 472.2 nm and comparing it to the measured difference, Fig. 9. It can be seen that the residuals between the calculated and measured phase difference when using Eqs. (7)–(9) (bottom row) are reduced by up to a factor of 4 compared to those produced when not accounting for the crystal misalignment (middle row). In addition, the prominence of the additional hyperbolic component in the fit residuals has been significantly reduced. The results shown in Fig. 9 have also been seen at the other four measured

TABLE I. Nominal and optimized instrument parameters for the MAST-U CIS system, where f_3 is the focal length of the system imaging lens and ρ is the orientation of a given component in the interferometer cell.

Parameter	Nominal	Optimized
f_3 (mm)	50	49.41
Component orientations		
ρ_{pol} (deg)	287.18	287.21
ρ_{disp} (deg)	264.68	260.43
ρ_{wp} (deg)	309.68	309.68
ρ_{qwp} (deg)	354.68	350.30

wavelengths, confirming that this method can be used to calibrate across a wide wavelength range. With this and the fact that the wavelength difference between CIII and Cd 467.82 nm is smaller than the test 472 nm line, we are confident that this method can be used to calibrate the instrument for C III at 464.7 nm. Despite good quantitative match shown, we cannot discount the possibility of an alternative underlying reason for this pattern. This would require further testing to confirm. As the modifications presented in this section increase the number of fitting parameters, we have seen up to a 20% increase in computational time. However, as this fitting is only required once per instrument installation, this increase will not have a significant effect on implementation.

IV. TEMPERATURE CHARACTERIZATION

Coherence imaging spectroscopy provides users with a powerful tool to measure plasma parameters in 2D; however, as shown in Sec. III, calibrating these systems can be challenging. The delay of birefringent crystals is dependent on temperature, typically attributed to a combination of the changes in the refractive indices, n_e and n_o (thermo-optic effect), and thermal expansion. In addition, we expect the temperature dependence of Φ_{2+1} and Φ_{2-1} to be equal to the sum and difference, respectively, of $\frac{d\phi}{dT}$ for each crystal. This issue has been mitigated on other devices through radial sightlines¹⁶

TABLE II. Nominal and optimized crystal specific parameters for the MAST-U CIS system. ψ_x and ψ_y are the tilts of each crystal about the x and y axes of the instrument, respectively. θ is the cut angle of the crystal, and A_e , B_e , C_e , and D_e are the Sellmeier coefficients of the crystal.

Parameter	Disp. plate		Waveplate	
	Nominal	Optimized	Nominal	Optimized
ψ_x (deg)	0	1.39	0	0.3726
ψ_y (deg)	0	-1.91	0	-0.6604
θ (deg)	45	45	0	-0.223
A_e (μm^2)	2.3753	2.3778	2.3753	2.3734
B_e (μm^2)	0.012 24	0.011 64	0.012 24	0.012 87
C_e (μm^2)	-0.016 67	-0.022 44	-0.016 67	-0.017 24
D_e (μm^2)	-0.016 67	-0.014 84	-0.015 16	-0.018 09

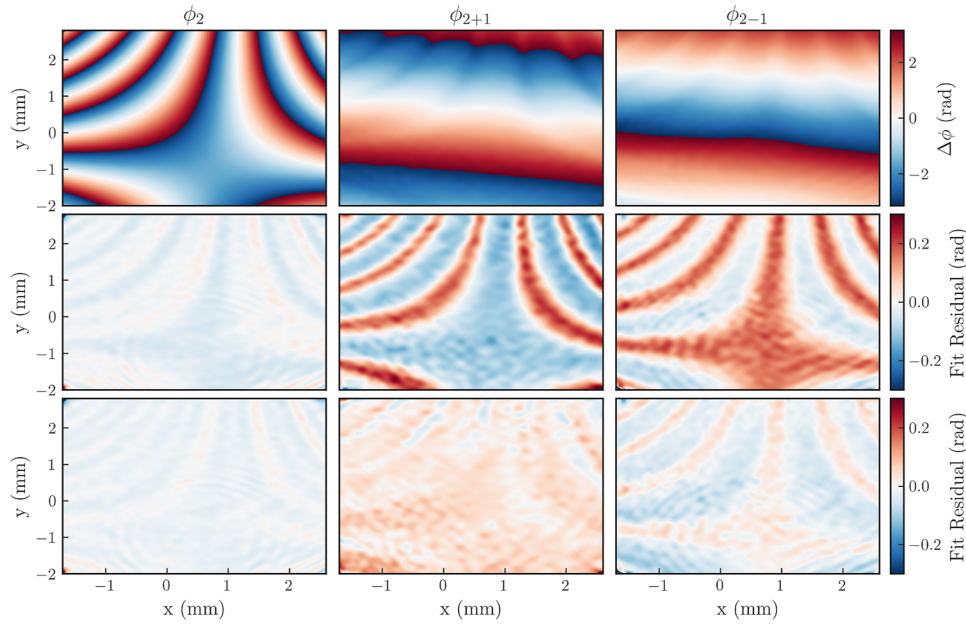


FIG. 9. The top row shows the difference in the phase images measured at 467.82 and 472 nm, where the ϕ_{2+1} and ϕ_{2-1} images clearly show an embedded hyperbolic pattern. The middle row shows the fit residuals when using the ideal equation for delay imparted by a linear retarder.²⁰ The final row shows fit residuals when using Eqs. (7)–(9).

or *in situ*^{18,22} calibration and precision temperature control.²² However, such solutions are not always practical and may become less reliable on devices capable of long pulse times. In the case of the MAST-U MWI, an *in situ* system was not practical due to the proximity of the front optics of the MWI to the vessel and other sensitive diagnostics. The method of assuming that the plasma is stationary along a given sightline¹⁶ can also not be used due to the viewing angles of the MWI front optics,

$$\frac{\Delta\phi_{0,n}}{\Delta T} \approx \phi_{0,n} \left(\alpha + \frac{1}{B_0} \frac{dB}{dT} \right), \quad (11)$$

$$L(T) = L_0 + L_0(\alpha_{\parallel} \sin \theta + \alpha_{\perp} \cos \theta) \Delta T, \quad (12)$$

$$n_e(T) = n_{e,0} + \frac{dn_e}{dT} \Delta T, \quad n_o(T) = n_{o,0} + \frac{dn_o}{dT} \Delta T. \quad (13)$$

To minimize this effect, all CIS components were installed in an Andover 50 mm Filter Oven, connected to the Andover DC Filter Oven Controller, which was set to $35^\circ \pm 0.2^\circ \text{C}$. Equation (11) describes the temperature dependence of the phase delay produced by a waveplate for light at normal incidence, based on the thermo-optic effect and thermal expansion,¹⁶ where α and $\frac{dB}{dT}$ are thermal constants and $B_0 = n_e - n_o$. Using Eq. (11) and thermal constants taken from the literature,²³ it can be estimated that an accuracy of $\pm 0.2^\circ$ in the crystal temperature stability corresponds to a phase stability on ϕ_2 of ± 0.19 rad. This is equivalent to a velocity of 3 km/s, which is large compared to the CIS accuracy of 1 km/s and measurements of < 30 km/s seen on MAST.^{16,24} In light of this, a new

method of calibrating the diagnostic to temperature changes was sought.

As Eq. (11) is only valid for a waveplate, ϕ_{2+1} and ϕ_{2-1} were calculated by combining the delay imparted by the displacer plate and the calculated delays for the waveplate. This was done by substituting Eqs. (12) and (13) into Eq. (4), where $\alpha_{\parallel, \perp}$ are the thermal expansion coefficients parallel and perpendicular to the optic axis of the crystal, θ is the cut-angle, and $\frac{dn_e}{dT} = -9.3 \times 10^{-6}/\text{K}$ and $\frac{dn_o}{dT} = -16.6 \times 10^{-6}/\text{K}$ are the thermo-optic coefficients as specified by the manufacturer. As the accuracy of the thermal constants is unknown, verification was sought by measuring the change in phase images, produced at 467.8 nm using a cadmium spectral lamp, over a period of 40 hours. Crystal temperatures were measured by affixing $100 \text{ k}\Omega \pm 1\%$ thermistors to the crystal mounts using an adhesive with a thermal conductivity close to that of α -BBO.

In Fig. 10, we show the mean phase change of a region at the center of each phase image over time. The data representing the displacer plate, ϕ_1 , were obtained by subtracting ϕ_2 from the measured ϕ_{2+1} and ϕ_{2-1} phase images. Also plotted is the change in the measured temperature of each crystal. We can see from the plot of ϕ_2 that using Eq. (4) and accounting for thermal effects, we can predict the change in the delay imparted by the waveplate to good accuracy. The small discrepancy observed can be attributed to errors in the thermal coefficients and the alignment of the crystal.

The same cannot be said for the change in the delay imparted by the displacer plate, which shows a strong disagreement between the calculated and measured. Reasonable modification of the thermal coefficients ($\pm 50\%$) did not provide good enough agreement to suggest errors in these as the sole cause. However, a change in the tilt

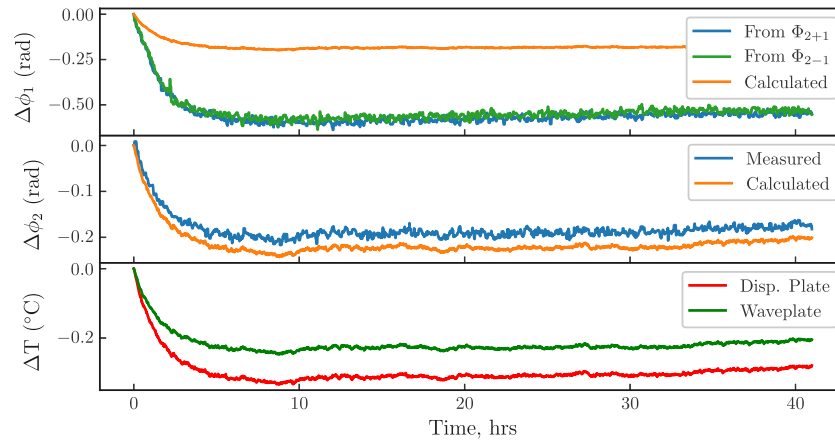


FIG. 10. Change in delay imparted by the displacer plate, ϕ_1 , and waveplate, ϕ_2 , with temperature as measured using a cadmium lamp and calculated using Eq. (4) accounting for thermal expansion and the thermo-optic effect.

of the displacer plate about the x and y axes on the order of 10^{-3} rad did provide a large enough change in the incidence angles to give quantitative agreement with individual pixel measurements. One possible cause of the discrepancy is crystal misalignment induced by thermal stresses between the crystal and its mount. Determining this as the cause would require a much more detailed study, which was not needed in this case,

$$\begin{aligned}\Phi_{1,i}(T) &= \phi_{0,1} + \Delta T \left[\frac{d\phi_1}{dT} + C_i \right], \\ \Phi_2(T) &= \phi_{0,2} + \Delta T \left[\frac{d\phi_2}{dT} + C_2 \right].\end{aligned}\quad (14)$$

It was found that a linear modification of the delay calculated using Eqs. (4), (12), and (13) through Eq. (14) would provide agreement with the measured data, where Φ is the measured phase

(i denotes which image ϕ_1 was calculated from), ϕ is the calculated phase at $\Delta T = 0$, C_i is a fitting parameter for each pixel, and $\frac{d\phi}{dT}$ is the change in phase due to thermal expansion and the thermo-optic effect.

Although ϕ_2 showed a good agreement with the measured data, it was decided to fit to ϕ_2 along with Φ_{2+1} and Φ_{2-1} , to correct for the small differences observed in Fig. 10. We believe that the small difference between $\Phi_{1,2+1}$ and $\Phi_{1,2-1}$, seen in Fig. 10, is due to how the additional hyperbolic pattern seen in Sec. III affects Φ_{2+1} and Φ_{2-1} . The technique described in Sec. III was not required here as by fitting to C_i at every pixel, all non-temperature dependent phenomena (such as errors due to misalignment) are captured by the fitting, as seen in Fig. 11,

$$\Phi_{2\pm 1}(T) = \phi_2(T) \pm \Phi_{1,2\pm 1}(T). \quad (15)$$

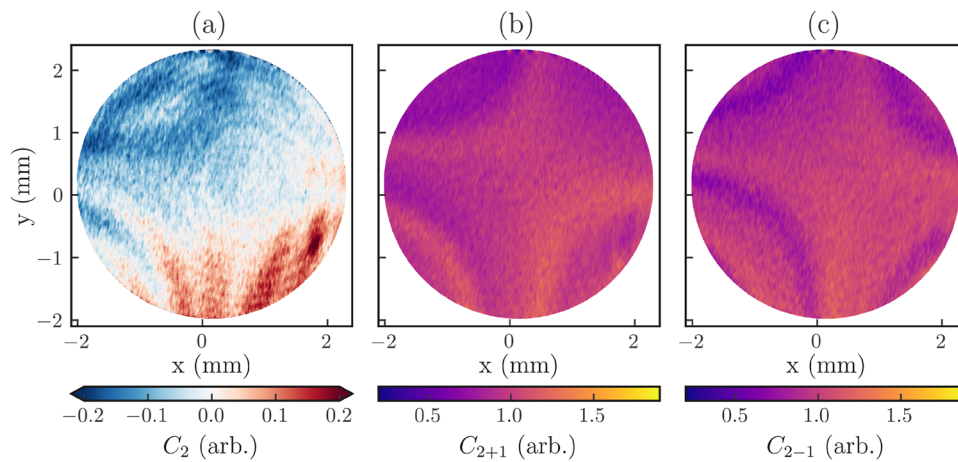


FIG. 11. Fitting parameter C_n plotted across the image circle. (a) Fitting done for ϕ_2 , (b) fitting done for ϕ_{2+1} , and (c) fitting done for ϕ_{2-1} .

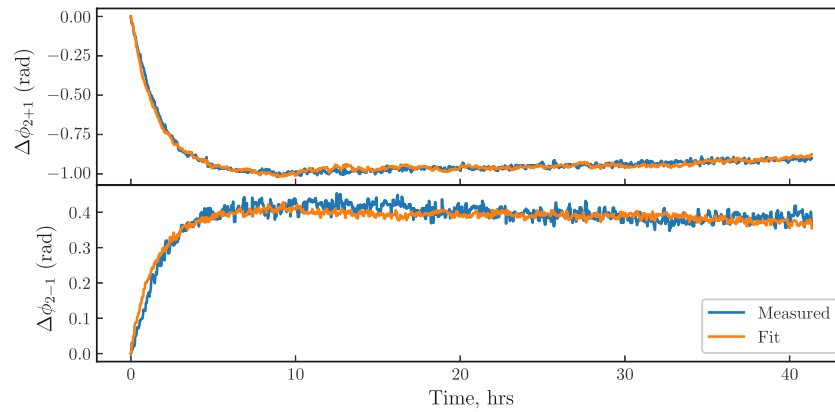


FIG. 12. A comparison between the change in the measured ϕ_{2+1} and ϕ_{2-1} terms with those calculated using Eq. (15).

Using Eq. (15), we can accurately predict the change in the measured ϕ_{2+1} and ϕ_{2-1} . Figure 12 shows a comparison of the mean measured variation and that calculated using Eq. (15) over the same region used in Fig. 10. It is clear from this that Eq. (15) can accurately account for the discrepancy seen in the predicted $\Delta\phi_1$ seen in Fig. 10.

Although the results in Fig. 12 are promising, they provide little information about whether Eq. (14) could be used as a way to generate CIS calibrations long-term using only crystal temperature. To test this, calibration images were taken nine days after the data in Fig. 12, during which temperature control was maintained and the instrument was left untouched. These data were compared to the phase images calculated using the crystal temperature at that time, as shown in Fig. 13.

It is clear from the residual images in Fig. 13 that Eq. (14) can be used to predict CIS calibration images to good accuracy, with absolute residual means of 0.013, 0.021, and 0.019 rad on Φ_2 , Φ_{2+1} , and Φ_{2-1} , respectively. This corresponds to a reduction in uncertainty for Φ_2 , when compared to that related to the temperature control cell's accuracy, of a factor of 15 and acceptable errors on the other two terms. It is important to note that the main source of discrepancy seen in Fig. 13 is noise, which can be mitigated in the future studies by stacking and averaging over a large set of frames taken at much lower exposure times. We can also see that residuals for Φ_{2+1} and Φ_{2-1} are of similar magnitude but opposite sign. This will be useful when applying calibrations to plasma experiments for physical studies, as these errors will partially cancel out.

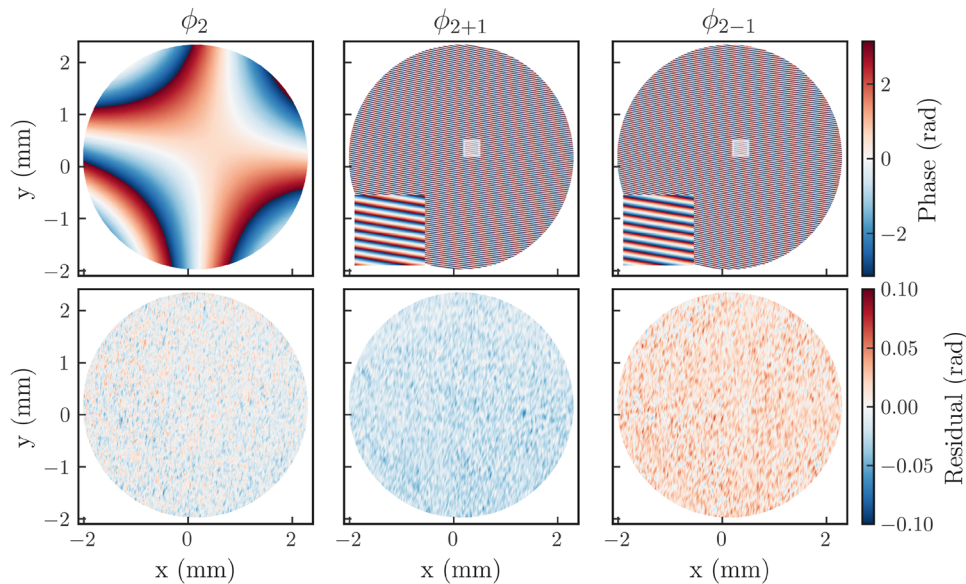


FIG. 13. Shown on the top row are Φ_2 , Φ_{2+1} , and Φ_{2-1} taken from measurements made nine days after the data that were fit to in Fig. 12. The bottom row shows the residual between the top row and the corresponding calculated phase images.

During this study, we confirmed that instrumental contrast is not strongly correlated with changes in crystal temperature, as seen by Silburn *et al.*¹⁶ A maximum variation of 0.015 was observed across the 40 hours, which is on the order of the contrast fluctuations attributed to noise in the measured interferogram. Therefore, for current studies on MAST-U, fitting between crystal temperature and instrumental contrast is not required. However, instrumental contrast will be measured at regular intervals to account for possible degradation of sensor polarizers due to neutron flux.

Adding this procedure in the installation workflow of a CIS instrument will have an effect on implementation time as measurements must be taken over an extended period. However, this process is not labor intensive and analysis can be done automatically within a few hours; therefore, we do not expect this to be an obstacle for future systems.

V. SUMMARY

In this paper, we have presented the changes made to the MAST-U MWI to accommodate the installation of a multi-delay coherence imaging system. Image ghosting due to beam splitter misalignment has been mitigated by installing the MWI spectral filter and beam splitter in the same optical holder. Issues with the collimation of light entering the CIS interferometer cell have been improved by changing the focal length of the collimating lens on channel 11 of the MWI from 750 to 600 mm, thus improving image focus and measured contrast.

In order to account for additional delay components observed when calibrating the system, we have extended previous work on fitting to the wavelength dependence of crystal delay. Our new equations for the measured phase, Eqs. (7)–(9), use the misalignment of interferometer components as a proxy for the observed effects; however, other physical processes may also contribute to this. It has been seen that by fitting to these equations, the additional hyperbolic component has been significantly reduced.

In addition, we present calibration procedures to account for the temperature and wavelength dependence of instrument delay. By measuring the temperature of each crystal using thermistors affixed to the crystal holder, we have shown that linear modification of Eq. (4), with thermal expansion and the thermo-optic effect accounted for, can effectively predict the temperature dependence of each crystal's imparted delay. This has resulted in negligible residuals primarily due to noise, which can be further improved by extending the measurement period and averaging over multiple images.

The combination of these techniques has allowed for effective calibration of the MAST-U coherence imaging diagnostic without the need for *in situ* calibration systems. The expected experimental uncertainties in phase have been reduced by up to a factor of 4 to ≤ 1 km/s for each delay, in velocity terms. As the relation between measured contrast and temperature/density is non-linear and errors are dominated by noise, uncertainties in temperature/density will vary with the contrast and signal-to-noise ratio measured at each pixel. For this reason, it is difficult to predict these errors; however, we do not expect uncertainties larger than that seen with similar

devices.⁸ It is important to note that the actual errors on velocity, temperature, and density measurements are likely to be lower than that for each individual phase/contrast image, as the use of multiple delays allows the user to better constrain results compared to single delay systems. This diagnostic will now be used to study impurity transport and temperatures, as well as electron densities in the MAST-U Super-X divertor.

ACKNOWLEDGMENTS

This work was carried out within the framework of the EUROfusion Consortium, funded by the European Union via the Euratom Research and Training Programme (Grant Agreement No. 101052200—EUROfusion) and from the EPSRC [Grant No. EP/W006839/1]. Views and opinions expressed are, however, those of the author(s) only and do not necessarily reflect those of the European Union or the European Commission. Neither the European Union nor the European Commission can be held responsible for them.

AUTHOR DECLARATIONS

Conflict of Interest

The authors have no conflicts to disclose.

Author Contributions

R. S. Doyle: Conceptualization (lead); Data curation (lead); Formal analysis (lead); Investigation (lead); Methodology (lead); Validation (lead); Visualization (lead); Writing – original draft (lead); Writing – review & editing (lead). **N. Lonigro:** Conceptualization (supporting); Data curation (supporting); Formal analysis (supporting); Writing – review & editing (supporting). **J. S. Allcock:** Conceptualization (supporting); Investigation (supporting); Methodology (supporting); Supervision (supporting); Writing – review & editing (supporting). **S. A. Silburn:** Conceptualization (supporting); Investigation (supporting); Methodology (supporting); Writing – review & editing (supporting). **M. M. Turner:** Funding acquisition (lead). **X. Feng:** Writing – review & editing (supporting). **H. Leggate:** Funding acquisition (supporting); Supervision (lead); Writing – review & editing (supporting).

DATA AVAILABILITY

The data that support the findings of this study are available from the corresponding author upon reasonable request.

APPENDIX A: MUELLER MATRICES

The Mueller matrix for a general linear retarder is given in Eq. (A1), where ϕ is the phase difference between the ordinary and extraordinary rays and ρ is the angle the fast-axis makes with the x-axis. For a quarter waveplate, the Mueller matrix can be obtained from $\mathbf{M}_{qwp}(\rho) = \mathbf{M}_{ret}(\rho, \frac{\pi}{2})$,

$$\mathbf{M}_{ret}(\rho, \phi) = \begin{bmatrix} 1 & 0 & 0 & 0 \\ 0 & \cos^2(2\rho) + \sin^2(2\rho) \cos(\phi) & \cos(2\rho) \sin(2\rho)(1 - \cos(\phi)) & \sin(2\rho) \sin(\phi) \\ 0 & \cos(2\rho) \sin(2\rho)(1 - \cos(\phi)) & \cos^2(2\rho) \cos(\phi) + \sin^2(2\rho) & -\cos(2\rho) \sin(\phi) \\ 0 & -\sin(2\rho) \sin(\phi) & \cos(2\rho) \sin(\phi) & \cos(\phi) \end{bmatrix}. \quad (\text{A1})$$

The Mueller matrix for a linear polarizer, where ρ is the angle the transmission axis makes with the x-axis, is given by

$$\mathbf{M}_{pol}(\rho) = \frac{1}{2} \begin{bmatrix} 1 & \cos(2\rho) & \sin(2\rho) & 0 \\ \cos(2\rho) & \cos^2(2\rho) & \cos(2\rho) \sin(2\rho) & 0 \\ \sin(2\rho) & \cos(2\rho) \sin(2\rho) & \sin^2(2\rho) & 0 \\ 0 & 0 & 0 & 0 \end{bmatrix}. \quad (\text{A2})$$

APPENDIX B: ANALYTICAL PHASE EQUATIONS

To derive Eqs. (7)–(9) through Mueller calculus, we will denote the misalignment of a component with the letter δ , the delay imparted by a given crystal is denoted by ϕ , the rotation of the interferometer cell with respect to the horizontal axis of the camera is denoted by θ_{rot} , and the Mueller matrix is a component, like above, which is denoted by \mathbf{M} .

The misalignment of a component is defined as the angular deviation of the fast-axis or transmission axis of that component from its ideal orientation ρ , as shown in Fig. 3(a). As the delay imparted by the waveplate in a triple delay is measured directly through Φ_2 , it is possible to determine the waveplate orientation ρ_{wp} ; therefore, the misalignment of the waveplate is said to be zero ($\delta_{wp} = 0$). From this, we can also determine the orientation of the interferometer cell, $\theta_{rot} = \rho_{wp} - \frac{\pi}{4}$.

We can then apply this to the matrices defined in Appendix A, where the Mueller matrix for the measured interferogram is now given by Eq. (B1), where ρ for each component is now $\rho + \delta + \theta_{rot}$. As δ is expected to be small for each component, we apply the small angle approximation to each term of the component's Mueller matrix,

$$\begin{aligned} \mathbf{M}_{tot} \equiv & \mathbf{M}_{pol}\left(m\frac{\pi}{4}\right) \times \mathbf{M}_{qwp}\left(\frac{\pi}{2} + \delta_{qwp} + \theta_{rot}\right) \\ & \times \mathbf{M}_{ret}\left(\frac{\pi}{4} + \theta_{rot}, \phi_2\right) \times \mathbf{M}_{ret}\left(0 + \delta_{disp} + \theta_{rot}, \phi_1\right) \\ & \times \mathbf{M}_{pol}\left(\frac{\pi}{8} + \delta_{pol} + \theta_{rot}\right). \end{aligned} \quad (\text{B1})$$

The interferogram equation I_{out} can then be obtained by multiplying \mathbf{M}_{tot} by the Stokes vector for unpolarized light $S_{in} = \{1, 0, 0, 0\}$ and taking the first term of the resultant vector. We then convert I_{out} to exponential form and multiply by $\exp(-im\frac{\pi}{4})$, replicating the demodulation of an interferogram.^{8,10} We can then neglect any high frequency terms and factor out the terms related

to each relevant delay (i.e., $e^{i\phi_1}$, $e^{i\phi_2}$, $e^{i\phi_{2+1}}$, $e^{i\phi_{2-1}}$), resulting in Eqs. (7)–(9).

REFERENCES

- P. M. Valanju, M. Kotschenreuther, S. M. Mahajan, and J. Canik, *Phys. Plasmas* **16**, 056110 (2009).
- D. Moulton, J. Harrison, B. Lipschultz, and D. Coster, *Plasma Phys. Controlled Fusion* **59**, 065011 (2017).
- B. Lipschultz, F. I. Parra, and I. H. Hutchinson, *Nucl. Fusion* **56**, 056007 (2016).
- W. Morris, J. R. Harrison, A. Kirk, B. Lipschultz, F. Militello, D. Moulton, and N. R. Walkden, *IEEE Trans. Plasma Sci.* **46**, 1217 (2018).
- X. Feng, A. Calcines, R. M. Sharples, B. Lipschultz, A. Perek, W. A. Vijvers, J. R. Harrison, J. S. Allcock, Y. Andrebe, B. P. Duval, and R. T. Mumgaard, *Rev. Sci. Instrum.* **92**, 063510 (2021).
- J. Howard, *Rev. Sci. Instrum.* **77**, 10F111 (2006).
- S. A. Silburn, "A Doppler coherence imaging diagnostic for the mega-Amp spherical tokamak," Ph.D. thesis, Durham University, 2014.
- J. S. Allcock, S. A. Silburn, R. M. Sharples, J. R. Harrison, N. J. Conway, and J. W. Vernimmen, *Rev. Sci. Instrum.* **92**, 073506 (2021).
- C. A. Michael, J. Howard, and B. D. Blackwell, *Phys. Plasmas* **11**, 4008 (2004).
- J. S. Allcock, "New techniques for coherence imaging fusion plasmas," Ph.D. thesis, Durham University, 2021.
- D. Gradic, V. Perseo, R. König, and D. Ennis, *Fusion Eng. Des.* **146**, 995 (2019).
- S. Allen, C. Samuelli, W. Meyer, A. Jaervinen, G. Porter, and T. Rognlien, *Nucl. Mater. Energy* **19**, 137 (2019).
- J. S. Allcock, S. A. Silburn, R. M. Sharples, J. R. Harrison, N. J. Conway, T. Long, and N. Lin, *Opt. Express* **31**(2), 1901–1915 (2023).
- J. Howard, *Appl. Opt.* **41**(1), 197–208 (2002).
- V. Perseo, D. Gradic, R. König, O. P. Ford, C. Killer, O. Grulke, D. A. Ennis, and W.-X. Team, *Rev. Sci. Instrum.* **91**, 013501 (2020).
- S. A. Silburn, J. R. Harrison, J. Howard, K. J. Gibson, H. Meyer, C. A. Michael, and R. M. Sharples, *Rev. Sci. Instrum.* **85**, 11D703 (2014).
- T. R. Weber, S. L. Allen, and J. Howard, *Rev. Sci. Instrum.* **83**, 10E102 (2012).
- D. Gradic, V. Perseo, D. Kriete, M. Krychowiak, R. König, Y. Feng, M. Otte, T. S. Pedersen, Y. Gao, M. Jakubowski, G. Schlisio, F. Warmer, and T. W7-X Team, *Nucl. Fusion* **61**, 106041 (2021).
- D. Gradic, O. P. Ford, A. Burckhart, F. Effenberg, H. Frerichs, R. König, T. Lunt, V. Perseo, and R. C. Wolf, *Plasma Phys. Controlled Fusion* **60**, 084007 (2018).
- F. E. Veiras, L. I. Perez, and M. T. Garea, *Appl. Opt.* **49**(15), 2769–2777 (2010).
- A. Perek, W. A. Vijvers, Y. Andrebe, I. G. Classen, B. P. Duval, C. Galperti, J. R. Harrison, B. L. Linehan, T. Ravensbergen, K. Verhaegh, and M. R. De Baar, *Rev. Sci. Instrum.* **90**, 102014 (2019).
- S. L. Allen, C. M. Samuelli, W. H. Meyer, and J. Howard, *Rev. Sci. Instrum.* **89**, 10E110 (2018).
- M. Duda, M. Dusek, O. Novák, and M. Smrž, in *Laser Congress 2021 (ASSL, LAC)* (Optica Publishing Group, 2021), p. JM3A34.
- I. Waters, H. Frerichs, S. Silburn, Y. Feng, J. Harrison, A. Kirk, and O. Schmitz, *Nucl. Fusion* **58**, 066002 (2018).